GDCh Research Article Angewandte International Edition Chemie www.angewandte.org

How to cite: *Angew. Chem. Int. Ed.* **2025**, e202515124
doi.org/10.1002/anie.202515124

Nanographenes

Symmetry-Engineered Ultralong Phosphorescence in Double π-Helical Nanographenes

Yujian Liu[+], Xu Wen[+], Xiao Chen, Jiangtao Chan, Zhigang Shuai, Zhaohui Wang, and Wei Jiang**

Abstract: The development of long-lived organic phosphorescent materials faces significant challenges in achieving precise control over triplet exciton emission processes. Herein, we present an innovative design strategy toward a novel class of double π-helical nanographenes (**8**–**10**) by integrating a chiral cyclooctahexaphenylene (COTh) core with diverse polycyclic aromatic hydrocarbons (PAHs). The process underwent sequential Knoevenagel condensation, Diels–Alder [4 + 2] cycloaddition, and final Scholl dehydrocyclization, using phenanthraquinone dimer **3** as the key chiral building block. By systematically varying the symmetry of PAH subunits from C_2 to C_{2v} to D_{6h}, we achieved remarkable orange-red phosphorescence with lifetimes (τ_p) reaching 5.5 s and afterglow durations up to 45 s at 77 K for **10** featuring highly D_{6h}-symmetric hexabenzocoronene (HBC) moieties. This exceptional performance stems from three synergistic effects in high-symmetry, rigid PAHs: (1) significantly suppressed $S_1 \rightarrow S_0$ radiative rates (k_f) due to symmetry-forbidden transitions governed by Clar's π-sextet rule, (2) extremely low triplet radiative decay (k_p), and (3) minimized nonradiative dissipation (k_{nr}). These double π-helical nanographenes further demonstrate tunable chiroptical properties, with absorption dissymmetry factor ($|g_{abs}|$) of 0.011 for **9** and exceptional Cotton effects ($\Delta\varepsilon = 457\ M^{-1}\ cm^{-1}$) for **10**. This research offers a valuable insight into the molecular design of chiral afterglow materials.

Introduction

Long-lived organic phosphorescence has emerged as a highly promising technology with broad applications in optical encryption, organic optoelectronics, and bioimaging.[1–10] To achieve persistent phosphorescence, three key parameters must be carefully balanced: (1) a rapid intersystem crossing (ISC) rate (k_{ISC}) to ensure efficient triplet exciton population; (2) a low triplet radiative decay rate (k_p) to prolong the phosphorescence lifetime; and (3) effective suppression of non-radiative pathways (k_{nr}) to enhance the phosphorescence quantum yield.[11,12] However, a fundamental trade-off exists between these requirements: functional groups containing lone-pair electrons (e.g., heteroatoms, carbonyls) or heavy atoms induce strong spin-orbit coupling (SOC), which significantly enhances ISC rates, but simultaneously accelerates k_p, thereby shortening phosphorescence lifetimes.[13,14] This inherent contradiction poses a major challenge in molecular design, as optimizing the balance between ISC efficiency and radiative decay suppression remains a critical yet elusive goal.

Polycyclic aromatic hydrocarbons (PAHs) have garnered long-standing research interest owing to their unique photophysical properties.[15–19] According to Clar's π-sextet rule, Clar-type PAHs exhibit symmetry-forbidden transitions in the $S_1 \rightarrow S_0$ radiative process, leading to significantly suppressed $S_1 \rightarrow S_0$ radiative rates ($k_f \sim 10^6\ s^{-1}$)—orders of magnitude lower than those of conventional fluorophores.[20,21] Since the k_p depends on both S_n–S_0 transition dipole moments and SOC effects,[13] these systems exhibit extremely low k_p values ($<10^{-1}\ s^{-1}$) that are at least eight orders of magnitude lower than their ISC rates ($k_{ISC} \sim 10^7\ s^{-1}$), highlighting their intrinsic potential for long-lived phosphorescence.[22–24] Recent advancements in nonplanar PAHs have unlocked new avenues for property modulation, enabling simultaneous control of electronic structures and circularly polarized phosphorescence.[25–30] Current strategies to impart chirality to PAH frameworks primarily involve the incorporation of helicene[31–40] or eight-membered cyclooctatetraene (COT)[41–44] subunits, which either distorts the planar geometry into a curved conformation or induces a spatially chiral arrangement of PAH units. While helicene-embedded PAHs exhibit improved chiroptical properties, their disrupted symmetry and extended π-conjugation often compromise the intrinsic photophysical properties of pristine PAHs.[45,46]

[*] Dr. Y. Liu[+], X. Wen[+], X. Chen, J. Chan, Prof. Dr. Z. Shuai, Prof. Dr. Z. Wang
Department of Chemistry, Key Laboratory of Organic Optoelectronics and Molecular Engineering, Tsinghua University, Beijing 100084, P.R. China
E-mail: wangzhaohui@mail.tsinghua.edu.cn

X. Wen[+], Prof. Dr. W. Jiang
School of Chemical Sciences, University of Chinese Academy of Sciences, Beijing 100049, P.R. China
E-mail: jiangw@ucas.ac.cn

Prof. Dr. Z. Shuai
School of Science and Engineering, The Chinese University of Hong Kong, Shenzhen, Guangdong 518172, P.R. China

[+] Both authors contributed equally to this work.

Additional supporting information can be found online in the Supporting Information section

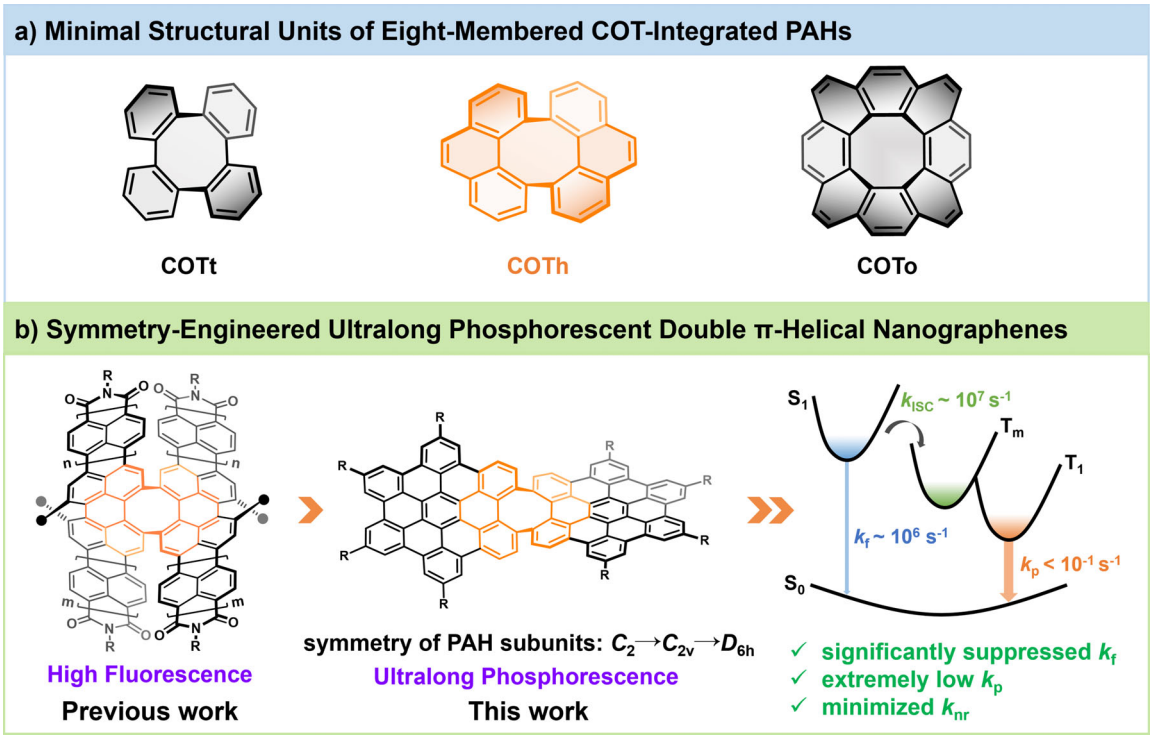

Figure 1. a) Minimal structural units of eight-membered COT-integrated PAHs. b) Our design concept of high fluorescent COTh-embedded double π-helices in our previous work and symmetry-engineered ultralong phosphorescent COTh-embedded double π-helical nanographenes in this work.

In contrast, the incorporation of COT rings minimally alters the electronic characteristics of PAHs and three typical minimal structural units of COT-integrated PAHs are cyclooctatetraphenylene (COTt), cyclooctahexaphenylene (COTh), and cyclooctaoctaphenylene (COTo), fusing with four, six, and eight benzene rings, respectively (Figure 1a). Among these, COTo, namely [8]circulene,[47] exhibits remarkable conformational flexibility that prevents chiral stereoisomer isolation due to rapid room temperature interconversion between twisted and saddle-shaped conformations, and COTt-embedded systems show limited chiroptical activity despite improved configurational stability.[42] The COTh architecture emerges as particularly promising and its double π-helical structure combines inherent chirality with a substantial isomerization barrier over 48 kcal mol^{-1}.[48] Our recent development of COTh-embedded double π-helices entwined with rylene diimide (RDI) units capitalizes on this framework, where the COTh core imposes near-orthogonal dihedral angles between adjacent RDI subunits.[49–53] This unique geometric constraint maintains weak interchromophoric conjugation (as evidenced by minimal spectral shifts compared to RDI monomer) while achieving both exceptional configurational stability (isomerization barrier up to 73 kcal mol^{-1}) and retention of RDI's excellent photophysical properties.[54–57] The resulting materials demonstrate outstanding circularly polarized luminescence (CPL) performance, featuring high fluorescence quantum yields (Φ_{FL} up to 95%) and impressive luminescence dissymmetry factors ($|g_{lum}|$ up to 0.03).

Building upon these fundamental insights, we present an innovative design strategy for ultralong phosphorescent double π-helical nanographenes by integrating a COTh chiral core with high-symmetry, rigid PAHs. This approach establishes a new paradigm for promising chiral afterglow materials while maintaining excellent emissive properties. Our design achieves three critical objectives: (1) significantly suppressed k_f to enhance the ISC process and triplet exciton population, (2) extremely low k_p, and (3) minimized k_{nr} due to the high molecular rigidity of PAHs (Figure 1b). The resulting COTh-embedded double π-helical nanographenes exhibit three remarkable characteristics: (1) near-orthogonal dihedral angles between PAH subunits lead to minimal interchromophoric conjugation, preserving emission properties nearly identical to the parent PAH skeleton; (2) ultralong phosphorescence with yellow (**9**: 25 s) and orange–red (**10**: 45 s) afterglow at 77 K; whilst the symmetry-breaking double π-helical nanographene **8** with C_2-symmetric PAH moieties achieves the highest Φ_{FL} of 31.7 %; (3) precisely tunable chiroptical properties through PAH subunits with different conjugation, with **9** reaching a maximum absorption dissymmetry factor ($|g_{abs}|$) of 0.011, and **10** exhibiting an outstanding Cotton effect ($\Delta\varepsilon = 457$ M^{-1} cm^{-1}).

Results and Discussion

Design and Synthesis

We initiated our synthesis by scaling up the production of phenanthrene dimer **2** (i.e., COTh) via a one-step palladium-mediated C—H activation of 4-chlorophenanthrene **1**, achiev-

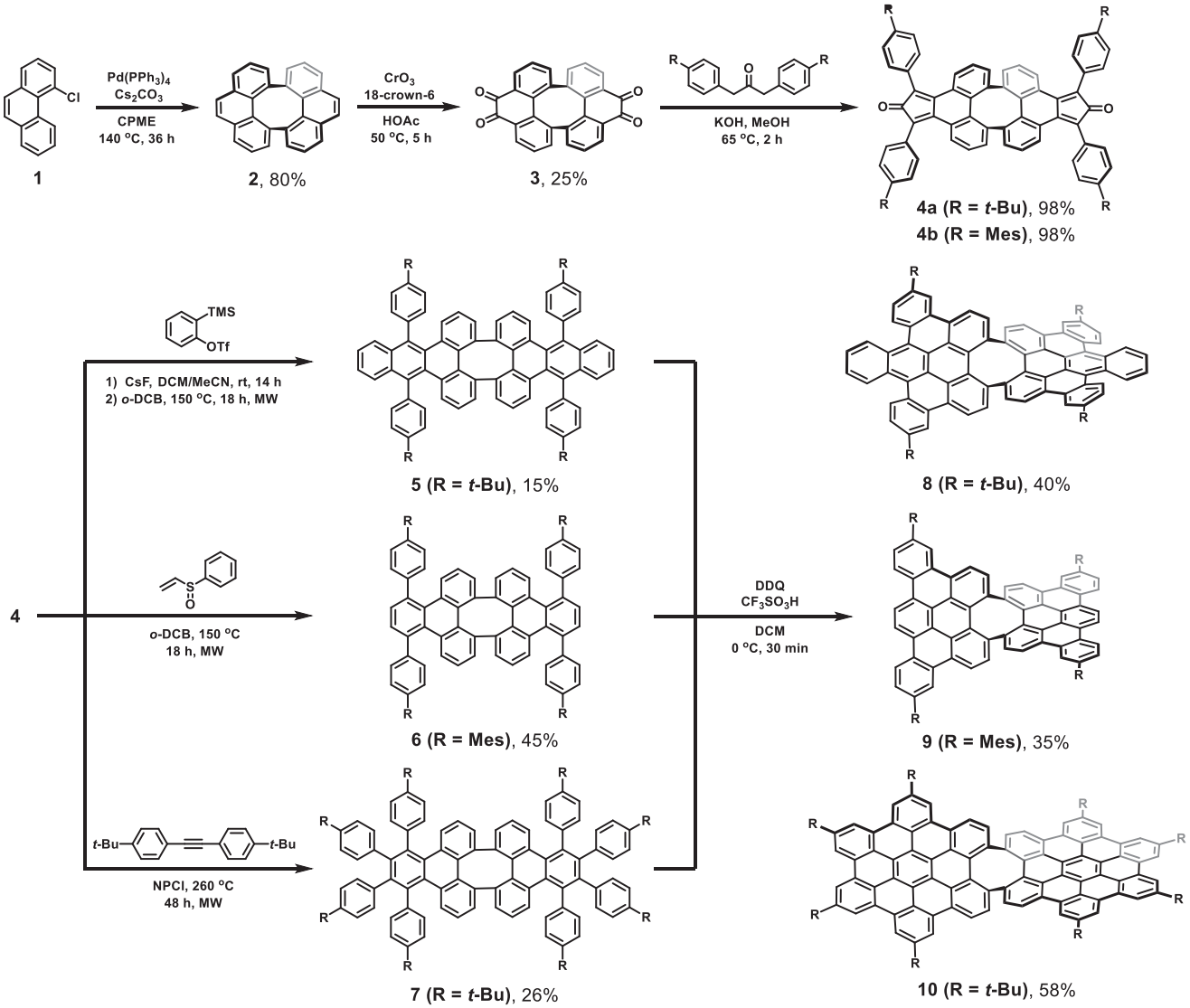

Scheme 1. Synthetic routes to COTh-embedded double π-helical nanographenes (**8**–**10**).

ing gram-scale quantities with approximately 80% yield following Itami's reported protocol.[48] The synthetic sequence then proceeded with oxidation of both *K*-regions in **2** using CrO_3/18-crown-6 to install 1,2-dicarbonyl functional groups, yielding the crucial chiral building block phenanthraquinone dimer **3**. This key intermediate was subsequently transformed through a Knoevenagel condensation with 1,3-diarylacetones to generate cyclopentadienone dimer **4**, which served as a versatile diene component in Diels–Alder [4 + 2] cycloadditions with various alkyne equivalents: 2-(trimethylsilyl)phenyl trifluoromethanesulfonate produced **5**, phenyl vinyl sulfoxide afforded **6**, and di(4-*tert*-butylphenyl)acetylene yielded **7**. Final Scholl dehydrocyclization reactions utlizing the DDQ/CF_3SO_3H system delivered the target double π-helical nanographenes (PAH dimers: **8**–**10**) in moderate yields (35%~58%, Scheme 1). Notably, the series demonstrates a deliberate subunits symmetry progression—**8** features lower C_2-symmetric PAH moieties showing symmetry-breaking character, **9** incorporates higher C_{2v}-symmetric tribenzoperylene (TBP) subunits, while **10** possesses the highest D_{6h}-symmetric hexabenzocoronene (HBC) fragments.

Structural Elucidation

We successfully obtained the single crystals of double π-helical nanographenes (**9** and **10**) and the parent COTh **2** suitable for X-ray diffraction analysis through slow evaporation crystallization using optimized solvent systems: $CHCl_3$/MeOH for **2**, CH_2Cl_2/$C_2H_4Cl_2$/cyclohexane for **9**, and chlorobenzene/CH_2Cl_2/EtOAc/MeOH for **10**.[58] X-ray crystallographic analysis revealed their distinct space groups: *Cc* for **2**, $P2_1/n$ for **9**, and *C*2/c for **10**. The crystal structures (Figure 2a–c) clearly demonstrate the double π-helical architecture, where two PAH subunits are elegantly entwined around the central COT ring (Figures S8–S10). Structural analysis uncovered significant geometric parameters: the tub-shaped distortion of the COT ring (θ_1) progressively

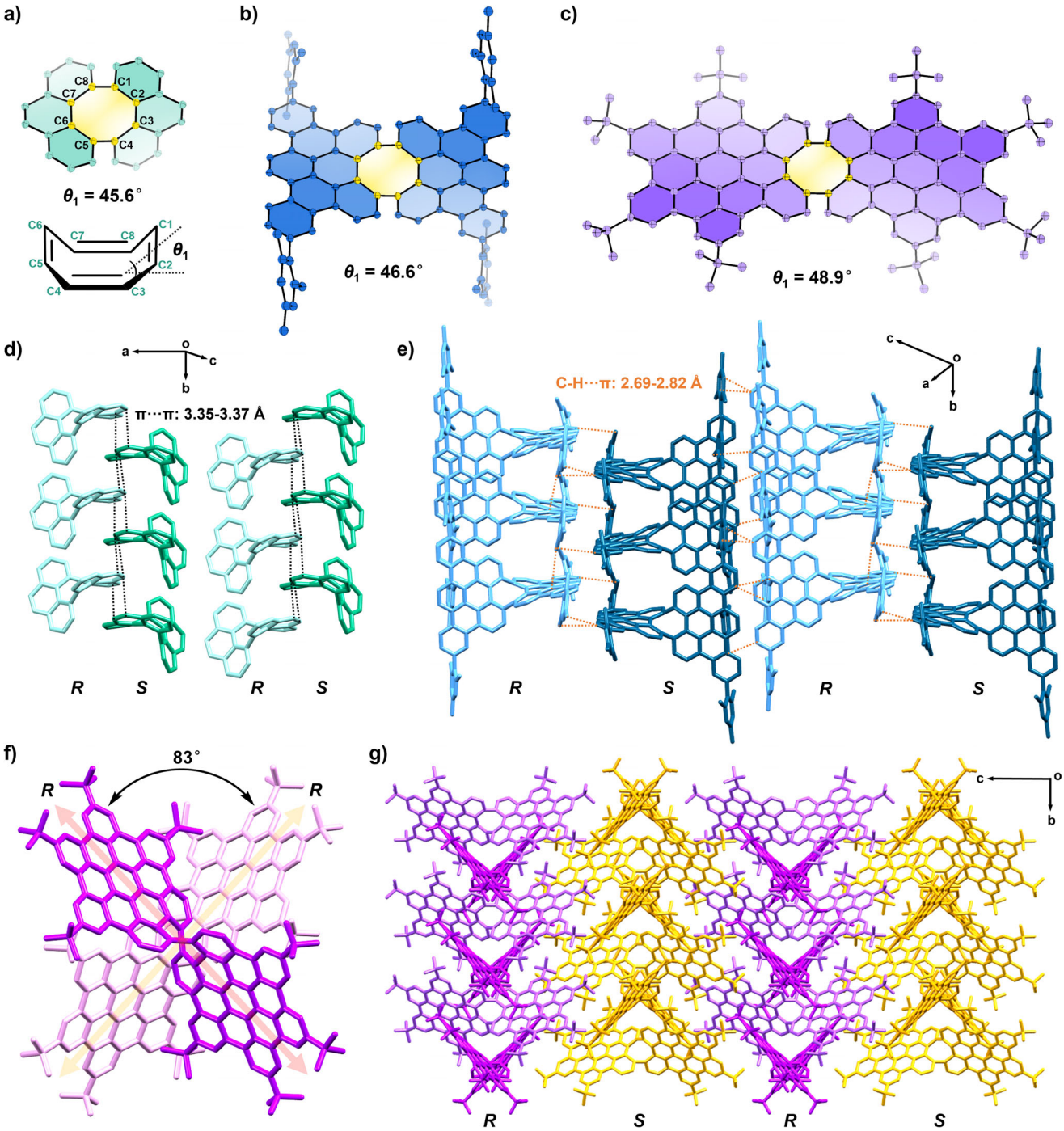

Figure 2. Single-crystal structures of **2**, **9,** and **10** with 50% thermal ellipsoid probability. Top views of a) *S*-**2**, b) *S*-**9**, and c) *S*-**10**. d) Packing arrangement of racemate **2** (the *R*- and *S*-enantiomer are depicted in light and dark green, respectively). e) Packing arrangement of racemate **9** (the *R*- and *S*-enantiomer are depicted in light and dark blue, respectively). f) Molecular columns arranged with homochiral isomers with rotating each other by ca. 83°. g) Packing arrangement of racemate **10** to form a homochiral lamellar and thus an achiral 3D crystal lattice (the *R*- and *S*-enantiomer are depicted in purple and yellow, respectively). The $\pi\cdots\pi$ and C—H$\cdots\pi$ interaction are indicated by the black and orange dotted line in d) and e), respectively. The H atoms are omitted for clarity.

increased from 45.6° (**2**) to 46.6° (**9**) and finally to 48.9° (**10**), demonstrating that extended π-conjugation enhances ring distortion. Furthermore, the near-orthogonal arrangement between PAH subunits was quantified by dihedral angles θ_2 of 87.7° (**9**) and 87.1° (**10**). These values represent a substantial increase compared to previously reported PDI-entwined COTh-embedded double π-helices (θ_1 = 42.6°, θ_2 = 74.7°),[49] confirming the more distorted geometry of the nanographene systems. The pronounced structural distortion effectively minimizes π-conjugation between PAH fragments, which crucially contributes to their distinctive photophysical characteristics.

Crystallographic analysis revealed distinct self-assembly patterns among the double π-helical nanographenes. The parent COTh **2** forms a 1D columnar supramolecular structure along the *b*-axis through homochiral segregation of *R*- and *S*-isomers, stabilized by C─H···π interactions (2.84–2.87 Å). The relatively small phenanthrene units facilitate additional heterochiral contacts, including both C─H···π interactions (2.76–2.82 Å) and π···π (3.35–3.37 Å) interactions, ultimately yielding a 3D superstructure network (Figure 2d). In contrast, double π-helical nanographenes **9** and **10** maintain homochiral segregation but exhibit more sophisticated packing motifs. The TBP dimer **9** organizes into well-defined columns where the bulky 2,4,6-trimethylphenyl (Mes) substituents engage in intra- and intercolumnar C─H···π interactions (2.69–2.82 Å), with dichloromethane solvent molecules precisely occupying interlamellar spaces through additional C─H···π contacts (2.63–2.79 Å) (Figure 2e and Figure S9). Most remarkably, HBC dimer **10** adopts an intricate assembly structure, characterized by swinging homochiral molecular columns that exhibit a relative rotation of approximately 83° between the adjacent molecules during formation (Figure 2f). This unique conformation primarily arises from intense C─H···π stacking interactions (2.49–2.89 Å) around the central COT rings due to the near-orthogonal orientation of the adjacent molecules. These unique homochiral columns further organize into a lamellar sheets in the *a*-*b* plane, which alternate between heterochiral lamellae to form an overall achiral 3D crystal lattice (Figure 2g and Figure S10).

Photophysical Properties

To elucidate the distinctive photophysical properties of these double π-helical nanographenes, we conducted UV–vis absorption spectra. As depicted in Figure 3a, these compounds demonstrate intricate, fine-structured absorption profiles spanning both UV and visible spectral regions. The absorption spectrum of **9** reveals characteristic PAH transitions at 316 nm (β-band), 380 nm (*p*-band), and 410 nm (α-band), consistent with Clar's aromatic sextet rule.[20,21] Notably, while both α- and *p*-bands are formally symmetry-forbidden transitions—explaining the weak intensity of the α-band (molar extinction coefficient: $\varepsilon = 1200\ M^{-1}\ cm^{-1}$) in **9** and the *p*-band gains observable intensity through vibronic coupling with the nearby β-absorption band. Compound **10**, containing the highest D_{6h}-symmetric HBC fragments, also exhibits optical inactivity of its α-band (450 nm, $\varepsilon = 2890\ M^{-1}\ cm^{-1}$) due to strict symmetry selection rules. However, its β-band (369 nm) and *p*-band (397 nm) display both enhanced intensities and pronounced red-shifts relative to **9**, reflecting the extended π-conjugation in this system. A striking contrast emerges when comparing spectral features across the series. Compound **8** has a less symmetric subunit structure (C_2) compared to the more symmetric TBP (C_{2v}). This lower symmetry allows certain light absorption events—normally "forbidden"—to now occur, resulting in greatly increased absorption strength at both its α-band (427 nm, $\varepsilon = 43\ 100\ M^{-1}\ cm^{-1}$) and *p*-band (405 nm). Finally, the strongest absorptions in all cases correspond to their β-bands, with the maximum molar extinction coefficients (ε_{max}) reaching 189 700 $M^{-1}\ cm^{-1}$ at 342 nm for **8**, 159 600 $M^{-1}\ cm^{-1}$ at 316 nm for **9**, and 237 700 $M^{-1}\ cm^{-1}$ at 369 nm for **10**. These systematic variations in absorption characteristics provide compelling evidence for how subunit symmetry and π-conjugation extent govern the electronic transitions in these architecturally complex nanographenes.

The emission spectra of dimers **9** and **10** exhibit well-resolved vibrational fine structures in the 400–500 nm and 450–600 nm ranges, respectively, characteristic of their highly rigid molecular framework. In striking contrast, the symmetry-breaking PAH dimer **8** shows a broad fluorescence profile with a vibrational maximum at 450 nm (Figure 3b). Structural analysis reveals that the chiral COT core maintains a rigid, twisted conformation that enforces near-orthogonal alignment between the two PAH subunits. This precise spatial arrangement effectively disrupts interchromophoric conjugation between adjacent subunits while preserving the intrinsic optical properties of the parent PAHs, thereby enabling efficient chirality propagation without compromising photophysical performance. We observed a pronouced symmetry-dependent Φ_{FL} trend: higher symmetric dimers **9** (7.7%) and **10** (5.0%) exhibit significantly quenched emission due to symmetry-forbidden transitions, while the symmetry-breaking analogue **8** achieves a remarkable Φ_{FL} enhancement up to 31.7%, all the photophysical measurements were conducted in toluene solutions. Complementary transient fluorescence studies provide kinetic evidence for this symmetry-breaking effect, revealing substantially suppressed radiative rates in higher subunit symmetric systems ($k_f = 6.6 \times 10^6\ s^{-1}$ for **9**; $3.4 \times 10^6\ s^{-1}$ for **10**) compared to the lower subunit symmetric molecule **8** ($k_f = 9.8 \times 10^7\ s^{-1}$) (Figure 3e). These quantitative measurements not only validate our symmetry-control strategy but also suggest that symmetry-forbidden transitions may promote triplet exciton population. Together, these comprehensive photophysical analyses establish subunit symmetry as a powerful design parameter for tuning the luminescent properties of double π-helical nanographenes.

Subsequently, low-temperature (77 K) phosphorescence studies of **8**–**10** revealed distinct emission characteristics correlated with subunit symmetry. The compounds exhibited phosphorescence maxima at 659 nm (**8**), 551 nm (**9**), and 631 nm (**10**), all significantly red-shifted from their corresponding fluorescence emissions (Figure 3c). Analysis of the singlet-triplet energy gaps (ΔE_{ST}) yielded values of 0.87 eV (**8**), 0.65 eV (**9**), and 0.56 eV (**10**), showing a clear trend of decreasing ΔE_{ST} with increasing subunit symmetry. The normalized prompt (ungated) emission spectra at 77 K showed that Clar's rule-obeying, dimers **9** and **10** displayed simultaneous fluorescence and phosphorescence emissions, with the highest D_{6h}-symmetric HBC dimer **10** exhibiting particularly strong phosphorescence intensity (Figure 3d). In stark contrast, the symmetry-breaking dimer **8** showed negligible phosphorescence, consistent with its much faster fluorescence rate (k_f) relative to intersystem crossing (k_{ISC}). Transient phosphorescence spectroscopy measurements (Figure 3f) quantified these differences, revealing phosphorescence lifetimes (τ_p) of 3.7 s (**9**) and 5.5 s (**10**), with emission tails extending to 800 nm, while **8** showed a markedly shorter τ_p of just 0.32 s.

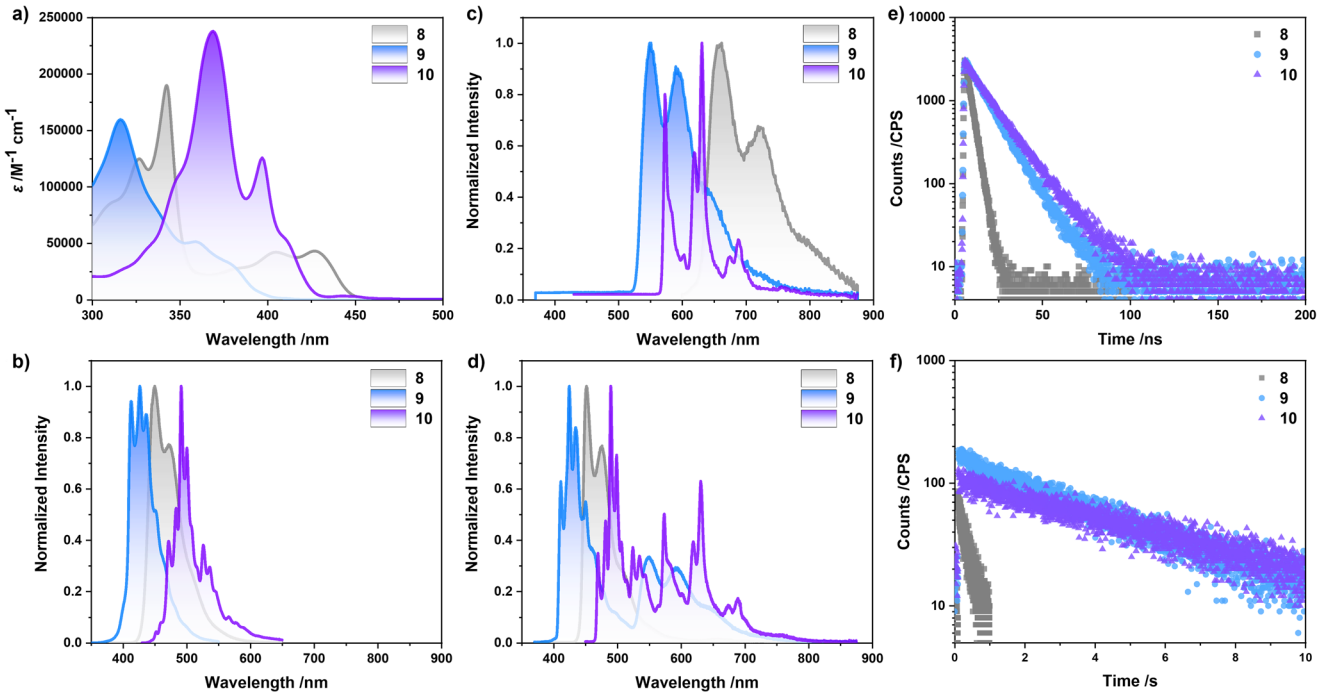

Figure 3. Photophysical properties of **8**, **9**, and **10** in toluene solutions (1×10^{-5} M). a) UV–vis absorption and. b) fluorescence spectra; c) phosphorescence spectra and. d) prompt luminescence spectra at 77 K under N_2 atmosphere; e) transient fluorescence decay spectra at room temperature under ambient atmosphere and f) transient phosphorescence decay spectra at 77 K under N_2 atmosphere.

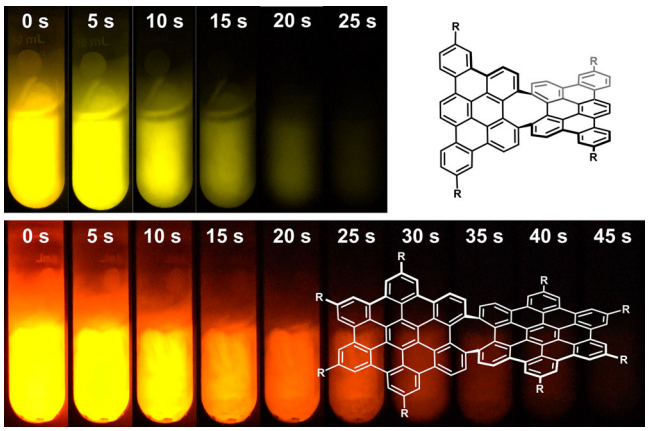

Figure 4. Photographs of phosphorescence for **9** (top) and **10** (bottom) in toluene solutions (1×10^{-4} M) at 77 K under N_2 atmosphere.

Notably, dimers **9** and **10** demonstrate ultralong phosphorescence afterglow durations of 25 s and 45 s, respectively, in toluene solutions at 77 K (Figure 4), with these experimental values showing excellent agreement with their corresponding τ_p measurements. Our comprehensive photophysical analysis, supported by Jablonski diagram simulations, reveals the underlying mechanism for this persistent luminescence: in the Clar's rule-compliant dimer **10**, the fluorescence radiative transition rate ($k_f \sim 10^6$ s^{-1}) is dramatically suppressed due to symmetry-forbidden transitions, falling approximately one order of magnitude below its intersystem crossing rate ($k_{ISC} \sim 10^7$ s^{-1}). The significantly suppressed k_f, combined with its large ΔE_{ST} and rigid molecular framework that effectively suppresses non-radiative decay from S_1 states, establishes a highly efficient exciton relaxation pathway: S_1 excitons preferentially undergo intersystem crossing to upper triplet states (T_m), followed by rapid internal conversion to the metastable T_1 state. The radiative transition rate for the triplet exciton (k_p) can be estimated using the following relationship:

$$k_p \propto \left|\overline{\mu_{T_1 \to S_0}}\right|^2 \tag{1}$$

$$\left|\overline{\mu_{T_1 \to S_0}}\right| = \sum_m \lambda_m \times \vec{\mu}_{S_m \to S_0} + \sum_n \lambda_m' \times \vec{\mu}_{T_m \to T_1} \tag{2}$$

$$\lambda_m = \frac{\left\langle \psi_1^{3(0)} | H_{SO} | \psi_m^{1(0)} \right\rangle}{{}^3E_1 - {}^1E_m}, \quad \lambda_m' = \frac{\left\langle \psi_m^{3(0)} | H_{SO} | \psi_0^{1(0)} \right\rangle}{{}^3E_m - {}^1E_0} \tag{3}$$

where $\mu_{T1 \to S0}$ is the transition dipole moment for the phosphorescence; $\mu_{Sm \to S0}$ is the transition dipole moment for the fluorescence that occurs from a n order singlet excited state (S_m) to S_0; $\Psi_m^{1(0)}$ is the electronic wavefunction of the $v = 0$ vibrational level of S_m; λ_m and λ_m' are the prohibition factors with respect to the SOC effect of the $T_1 \to S_0$ transition; Hso is the SOC operator; ${}^3E_1 - {}^1E_m$ is the energy difference between T_1 and S_m; and ${}^3E_m - {}^1E_0$ is the energy difference between T_m and S_0.[13]

The aforementioned equation reveals that k_p is principally determined by the $T_1 \to S_0$ transition dipole moment ($\mu_{T1 \to S0}$),[59] which is predominantly influenced by the first term in Equation (2), due to relatively small T_1-S_m energy gap. Three key factors contribute to the exceptionally low k_p values ($<10^{-1}$ s^{-1}) observed in these systems: first, the

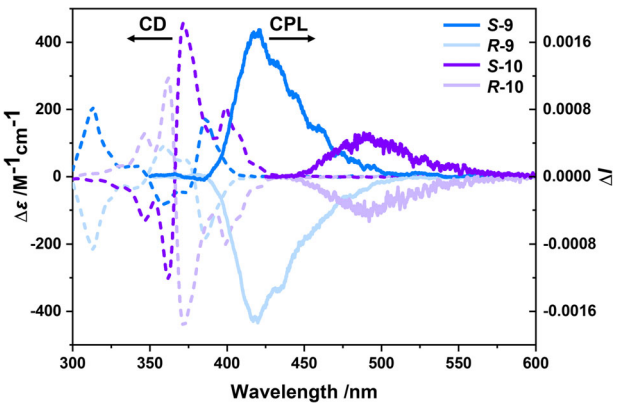

Figure 5. CD spectra and CPL emission spectra of **9** and **10** in toluene solutions (1×10^{-5} M).

SOC effect is inherently weak in all-carbon PAH derivatives due to the absence of heavy atoms; second, their large ΔE_{ST} values lead to minimal λ_m; third, symmetry-forbidden transitions dramatically suppress the singlet radiative transition dipole moments ($\mu_{Sm\rightarrow S0}$). Crucially, since the first term in Equation (2) represents the product of λ_m and $\mu_{Sm\rightarrow S0}$, these combined effects result in k_p values ($<10^{-1}$ s^{-1}) that are approximately eight orders of magnitude smaller than their corresponding k_{ISC} ($\sim 10^7$ s^{-1}), thereby enabling the observed ultralong afterglow phenomenon. In marked contrast, the symmetry-breaking **8** elevates its k_f close to 10^8 s^{-1}, substantially exceeding its k_{ISC}, thereby favoring S_1 exciton relaxation through radiative fluorescence pathways. Moreover, the enhanced $\mu_{Sm\rightarrow S0}$ in this asymmetric system leads to significantly increased k_p, ultimately manifesting as a substantially reduced τ_p value. This striking comparison between higher and lower symmetric systems quantitatively demonstrates how subunit symmetry governs the competition between radiative and non-radiative relaxation pathways in nanographene-based emitters.

Chiroptical Response

We next examined the chiroptical properties of two pairs of isolated enantiomers (**9** and **10**) in toluene solutions (1×10^{-5} M). As illustrated in Figure 5, both enantiomeric pairs display strong Cotton effects that precisely correspond to their UV–vis absorption spectra. The maximum $\Delta\varepsilon$ values consistently correlate with the β-absorption bands, exhibiting a systematic enhancement from 215 M^{-1} cm^{-1} at 313 nm for **9** to 457 M^{-1} cm^{-1} at 372 nm for **10**—a trend that parallels the red-shift and intensification of absorption with extended π-conjugation. According to equation $g_{abs} = \Delta\varepsilon/\varepsilon$, the maximum absorption dissymmetry factor ($|g_{abs}|$) of **9** was determined to be 0.011 at 394 nm. Upon further annulation, the $|g_{abs}|$ value of **10** decreased to 2.2×10^{-3} at 407 nm. Excellent agreement between experimental and theoretical CD spectra enabled unambiguous configurational assignment of these double π-helical architectures. Subsequently, CPL spectra were measured to assess their chiroptical performance in the excited states. Analogous to the CD properties, the two pairs of enantiomers display perfect mirror-image characteristics in the CPL spectra plots, which are consistent with the fluorescence spectra. The intensities of the CPL spectra show a similar trend as the ($|g_{lum}|$) changes. Specifically, the maximum $|g_{lum}|$ values reach up to 4.3×10^{-3} (406 nm) for **9** and 1×10^{-3} (492 nm) for **10**.

To deduce the structural origin of the observed g values, we conducted time-dependent density functional theory (TDDFT) calculations at the PBE0/def2-SVP level to analyze the electric ($\boldsymbol{\mu}$) and magnetic ($\boldsymbol{m}$) transition dipole moments, along with their mutual angles (θ), for relevant electronic transitions ($S_0\rightarrow S_n$).[60,61] The *S*-**9** and *S*-**10** are arbitrarily chosen. Our calculations reveal that these COTh-embedded double π-helical nanographenes possess globally D_2 molecular symmetry, resulting in transition dipole moment vectors that are either parallel or antiparallel in both the ground and excited states ($|\cos\theta| = 1$). Applying the simplified formula: $g = 4\cos\theta|\boldsymbol{m}|/|\boldsymbol{\mu}|$,[62] we found that the maximum theoretical $|g_{abs}|$ value for *S*-**9** (2.9×10^{-2}), arising from the $S_0\rightarrow S_1$ transition, shows excellent agreement with experimental measurements. In contrast, *S*-**10** exhibits two nearly degenerate excited states ($S_0\rightarrow S_3$ and $S_0\rightarrow S_4$) with opposing CD signals, which partially cancel each other and consequently reduce the overall dissymmetry factor.

Conclusion

In summary, we have developed a novel class of PAH-entwined double π-helices by integrating a COTh core with diverse PAH subunits. The synthetic approach employs phenanthrenequinone dimer (**3**) as a key chiral building block, which undergoes sequential Knoevenagel condensation, Diels–Alder [4 + 2] cycloaddition, and final Scholl dehydrocyclization to construct the target double π-helical nanographenes (**8**–**10**). This molecular design successfully incorporates chirality while maintaining the excellent photophysical characteristics of the parent PAHs. The double π-helical nanographenes **9** and **10**, comprising higher C_{2v} and D_{6h} symmetric PAH subunits, demonstrated remarkable afterglow durations of 25 and 45 s at 77 K, respectively. Whilst **8** with symmetry-breaking PAH moieties showed superior fluorescence quantum yield (Φ_{FL} = 31.7%) but negligible phosphorescence. Comprehensive analyses revealed three synergistic factors enabling the ultralong afterglow: (1) significantly suppressed $S_1\rightarrow S_0$ radiative rates due to symmetry-forbidden transitions, (2) diminished SOC effect resulting from the all-carbon composition, and (3) rigid molecular frameworks that effectively minimized non-radiative decay. Furthermore, CD and CPL spectroscopy proved precise modulation of chiroptical properties through PAH subunits with different conjugation. These findings establish fundamental design principles for chiral phosphorescent materials.

Supporting Information

The authors have cited additional references within the Supporting Information.

Acknowledgements

This work was financially supported by the National Natural Science Foundation of China (NSFC) (Nos. 22350005, 22235005, 22275112, and 22461160284), and the Fundamental Research Funds for the Central Universities (E5EQ0301X2).

Conflict of Interests

The authors declare no conflict of interest.

Data Availability Statement

The data that support the findings of this study are available in the Supporting Information of this article.

Keywords: Chirality · Double π-helical nanographenes · Long-lived phosphorescence · Polycyclic aromatic hydrocarbons · Symmetry-forbidden transitions

[1] B. Chang, J. Chen, J. Bao, T. Sun, Z. Cheng, *Chem. Rev.* **2023**, *123*, 13966–14037.
[2] W. Zhao, Z. He, B. Z. Tang, *Nat. Rev. Mater.* **2020**, *5*, 869–885.
[3] X. Ma, J. Wang, H. Tian, *Acc. Chem. Res.* **2019**, *52*, 738–748.
[4] R. Kabe, N. Notsuka, K. Yoshida, C. Adachi, *Adv. Mater.* **2016**, *28*, 655–660.
[5] X. Yang, G. I. N. Waterhouse, S. Lu, J. Yu, *Chem. Soc. Rev.* **2023**, *52*, 8005–8058.
[6] W. Ye, H. Ma, H. Shi, H. Wang, A. Lv, L. Bian, M. Zhang, C. Ma, K. Ling, M. Gu, Y. Mao, X. Yao, C. Gao, K. Shen, W. Jia, J. Zhi, S. Cai, Z. Song, J. Li, Y. Zhang, S. Lu, K. Liu, C. Dong, Q. Wang, Y. Zhou, W. Yao, Y. Zhang, H. Zhang, Z. Zhang, X. Hang, Z. An, X. Liu, W. Huang, *Nat. Mater.* **2021**, *20*, 1539–1544.
[7] C. Si, T. Wang, A. K. Gupta, D. B. Cordes, A. M. Z. Slawin, J. S. Siegel, E. Zysman-Colman, *Angew. Chem. Int. Ed.* **2023**, *62*, e202309718.
[8] G. Zhang, G. M. Palmer, M. W. Dewhirst, C. L. Fraser, *Nat. Mater.* **2009**, *8*, 747–751.
[9] W.-L. Zhou, Y. Chen, Q. Yu, H. Zhang, Z.-X. Liu, X.-Y. Dai, J.-J. Li, Y. Liu, *Nat. Commun.* **2020**, *11*, 4655.
[10] J. Li, Y. Guan, T.-T. Hao, J. Huang, Y. Chen, H. Li, P. Duan, H.-L. Xie, *Angew. Chem. Int. Ed.* **2025**, *64*, e202423395.
[11] D. Zhang, M. Li, C. Chen, *Sci. China Mater.* **2023**, *66*, 4030–4036.
[12] J. Liu, X. Zhou, X. Tang, Y. Tang, J. Wu, Z. Song, H. Jiang, Y. Ma, B. Li, Y. Lu, Q. Li, *Adv. Funct. Mater.* **2025**, *35*, 2414086.
[13] S. Hirata, *Adv. Opt. Mater.* **2017**, *5*, 1700116.
[14] Y. Zhang, X. Chen, J. Xu, Q. Zhang, L. Gao, Z. Wang, L. Qu, K. Wang, Y. Li, Z. Cai, Y. Zhao, C. Yang, *J. Am. Chem. Soc.* **2022**, *144*, 6107–6117.
[15] J. Wu, W. Pisula, K. Müllen, *Chem. Rev.* **2007**, *107*, 718–747.
[16] S. Ramírez-Barroso, F. Romeo-Gella, J. M. Fernández-García, S. Feng, L. Martínez-Fernández, D. García-Fresnadillo, I. Corral, N. Martín, R. Wannemacher, *Adv. Mater.* **2023**, *35*, 2212064.
[17] A. Narita, X.-Y. Wang, X. Feng, K. Müllen, *Chem. Soc. Rev.* **2015**, *44*, 6616–6643.
[18] W. Jiang, Z. Wang, *J. Am. Chem. Soc.* **2022**, *144*, 14976–14991.
[19] M.-W. Wang, W. Fan, X. Li, Y. Liu, Z. Li, W. Jiang, J. Wu, Z. Wang, *ACS Nano* **2023**, *17*, 20734–20752.
[20] H. B. Klevens, J. R. Platt, *J. Chem. Phys.* **1949**, *17*, 742–742.
[21] R. Rieger, K. Müllen, *J. Phys. Org. Chem.* **2010**, *23*, 315–325.
[22] J. L. Kropp, W. R. Dawson, *J. Phys. Chem.* **1967**, *71*, 4499–4506.
[23] S. Hirata, M. Vacha, *Adv. Opt. Mater.* **2017**, *5*, 1600996.
[24] X. Zheng, Q. Han, Q. Lin, C. Li, J. Jiang, Q. Guo, X. Ye, W. Z. Yuan, Y. Liu, X. Tao, *Mater. Horiz.* **2023**, *10*, 197–208.
[25] D. Lu, G. Zhuang, H. Wu, S. Wang, S. Yang, P. Du, *Angew. Chem. Int. Ed.* **2017**, *56*, 158–162.
[26] J. Fernández-García, P. Evans, S. Rivero, I. Fernández, D. García-Fresnadillo, J. Perles, J. Casado, N. Martín, *J. Am. Chem. Soc.* **2018**, *140*, 17188–17196.
[27] S. Ma, J. Gu, C. Lin, Z. Luo, Y. Zhu, J. Wang, *J. Am. Chem. Soc.* **2020**, *142*, 16887–16893.
[28] P. Izquierdo-García, J. Fernández-García, I. Fernández, J. Perles, N. Martín, *J. Am. Chem. Soc.* **2021**, *143*, 11864–11870.
[29] X. Liu, Z. Jin, F. Qiu, Y. Guo, Y. Chen, Z. Sun, L. Zhang, *Angew. Chem. Int. Ed.* **2024**, *63*, e202407547.
[30] V. Kumar, G. Venugopal, A. B. Jadhav, S. D. Dongre, R. Gonnade, J. Kumar, P. C. Ruer, B. Hupp, A. Steffen, S. S. Babu, *Angew. Chem. Int. Ed.* **2025**, *64*, e202422125.
[31] D. Meng, H. Fu, C. Xiao, X. Meng, T. Winands, W. Ma, W. Wei, B. Fan, L. Huo, N. L. Doltsinis, Y. Li, Y. Sun, Z. Wang, *J. Am. Chem. Soc.* **2016**, *138*, 10184–10190.
[32] G. Liu, T. Koch, Y. Li, N. L. Doltsinis, Z. Wang, *Angew. Chem. Int. Ed.* **2019**, *58*, 178–183.
[33] D. Meng, G. Liu, C. Xiao, Y. Shi, L. Zhang, L. Jiang, K. K. Baldridge, Y. Li, J. S. Siegel, Z. Wang, *J. Am. Chem. Soc.* **2019**, *141*, 5402–5408.
[34] G. Liu, Y. Liu, C. Zhao, Y. Li, Z. Wang, H. Tian, *Angew. Chem. Int. Ed.* **2023**, *62*, e202214769.
[35] Z. Qiu, C. Ju, L. Frédéric, Y. Hu, D. Schollmeyer, G. Pieters, K. Müllen, A. Narita, *J. Am. Chem. Soc.* **2021**, *143*, 4661–4667.
[36] J. Li, X. Chen, Y. Guo, X. Wang, A. Sue, X. Cao, X. Wang, *J. Am. Chem. Soc.* **2021**, *143*, 17958–17963.
[37] P. Izquierdo-García, J. Fernández-García, S. Medina Rivero, M. Šámal, J. Rybáček, L. Bednárová, S. Ramírez-Barroso, F. J. Ramírez, R. Rodríguez, J. Perles, D. García-Fresnadillo, J. Crassous, J. Casado, I. G. Stará, N. Martín, *J. Am. Chem. Soc.* **2023**, *145*, 11599–11610.
[38] W. Niu, Y. Fu, Z.-L. Qiu, C. J. Schürmann, S. Obermann, F. Liu, A. A. Popov, H. Komber, J. Ma, X. Feng, *J. Am. Chem. Soc.* **2023**, *145*, 26824–26832.
[39] Y.-J. Shen, N.-T. Yao, L.-N. Diao, Y. Yang, X.-L. Chen, H.-Y. Gong, *Angew. Chem. Int. Ed.* **2023**, *62*, e202300840.
[40] F. Morita, Y. Kishida, Y. Sato, H. Sugiyama, M. Abekura, J. Nogami, N. Toriumi, Y. Nagashima, T. Kinoshita, G. Fukuhara, M. Uchiyama, H. Uekusa, K. Tanaka, *Nat. Synth.* **2024**, *3*, 774–786.
[41] K. Y. Cheung, C. K. Chan, Z. Liu, Q. Miao, *Angew. Chem. Int. Ed.* **2017**, *56*, 9003–9007.
[42] J. Urieta-Mora, M. Krug, W. Alex, J. Perles, I. Fernández, A. Molina-Ontoria, D. M. Guldi, N. Martín, *J. Am. Chem. Soc.* **2020**, *142*, 4162–4172.
[43] M. A. Medel, R. Tapia, V. Blanco, D. Miguel, S. P. Morcillo, A. G. Campaña, *Angew. Chem. Int. Ed.* **2021**, *60*, 6094–6100.
[44] J. Liu, J. Hong, Z. Liao, J. Tan, H. Liu, E. Dmitrieva, L. Zhou, J. Ren, X.-Y. Cao, A. A. Popov, Y. Zou, A. Narita, Y. Hu, *Angew. Chem. Int. Ed.* **2024**, *63*, e202400172.
[45] D. Reger, P. Haines, F. W. Heinemann, D. M. Guldi, N. Jux, *Angew. Chem. Int. Ed.* **2018**, *57*, 5938–5942.
[46] N. J. Schuster, D. W. Paley, S. Jockusch, F. Ng, M. L. Steigerwald, C. Nuckolls, *Angew. Chem. Int. Ed.* **2016**, *55*, 13519–13523.
[47] Y. Sakamoto, T. Suzuki, *J. Am. Chem. Soc.* **2013**, *135*, 14074–14077.
[48] S. Matsubara, Y. Koga, Y. Segawa, K. Murakami, K. Itami, *Nat. Catal.* **2020**, *3*, 710–718.
[49] Y. Liu, Z. Ma, Z. Wang, W. Jiang, *J. Am. Chem. Soc.* **2022**, *144*, 11397–11404.

[50] Z. Ma, Q. Sun, J. Zhou, Y. Liu, Z. Shuai, Z. Wang, W. Jiang, *ACS Mater. Lett.* **2023**, *5*, 450–457.
[51] Y. Liu, Z. Li, M.-W. Wang, J. Chan, G. Liu, Z. Wang, W. Jiang, *J. Am. Chem. Soc.* **2024**, *146*, 5295–5304.
[52] K. Chen, Y. Liu, Z. Wang, S. Hu, Y. Zhao, W. Wang, G. Liu, Z. Wang, W. Jiang, *J. Am. Chem. Soc.* **2024**, *146*, 13499–13508.
[53] Y. Zhang, Y. Liu, W. Jiang, Z. Wang, *Acc. Mater. Res.* **2025**, *6*, 158–171.
[54] J. M. Fernández-García, P. Izquierdo-García, M. Buendía, S. Filippone, N. Martín, *Chem. Commun.* **2022**, *58*, 2634–2645.
[55] S. E. Penty, M. A. Zwijnenburg, G. R. F. Orton, P. Stachelek, R. Pal, Y. Xie, S. L. Griffin, T. A. Barendt, *J. Am. Chem. Soc.* **2022**, *144*, 12290–12298.
[56] J. Li, P. Li, M. Fan, X. Zheng, J. Guan, M. Yin, *Angew. Chem. Int. Ed.* **2022**, *61*, e202202532.
[57] D. P. Sukumaran, K. Shoyama, R. K. Dubey, F. Würthner, *J. Am. Chem. Soc.* **2024**, *146*, 22077-22084.
[58] Deposition numbers 2424761 (for **2**), 2426439 (for **9**), and 2424763 (for **10**) contain the supplementary crystallographic data for this paper. These data are provided free of charge by the joint Cambridge Crystallographic Data Centre and Fachinformationszentrum Karlsruhe Access Structures service.
[59] H. Ma, W. Shi, J. Ren, W. Li, Q. Peng, Z. Shuai, *J. Phys. Chem. Lett.* **2016**, *7*, 2893–2898.
[60] C. Adamo, V. Barone, *J. Chem. Phys.* **1999**, *110*, 6158–6170.
[61] F. Weigend, R. Ahlrichs, *Phys. Chem. Chem. Phys.* **2005**, *7*, 3297–3305.
[62] T. Mori, *Chem. Rev.* **2021**, *121*, 2373–2412.

Manuscript received: July 11, 2025
Revised manuscript received: September 25, 2025
Manuscript accepted: September 26, 2025
Version of record online: ■■, ■■